Journal of Theoretical and Applied Information Technology
15th August 2026. Vol.104. No.15

ISSN: 1992-8645 www.jatit.org E-ISSN: 1817-3195

SLGT-NET: AN EXPLAINABLE STACKED TABNET–LIGHTGBM FRAMEWORK FOR LUNG NODULE CLASSIFICATION FROM CT AND MRI IMAGES

SHEIK JAMIL AHMED[1] , VISHWANATH Y.[2*], SAIRA BANU ATHAM[3]

[1]Research Scholar, Presidency School of Computer Science and Engineering, Presidency University, Bangalore, Karnataka, India

[2*]Professor, Presidency School of Computer Science and Engineering, Presidency University, Bangalore, Karnataka, India

[3]Professor, Department of Computer Science and Engineering, Aurora University, Hyderabad, Telangana, India

E-mail: [1]jamil.20223cse0045@presidencyuniversity.in, [2*]vishwanath.y@presidencyuniversity.in, [3]saira.atham@gmail.com

ABSTRACT

Early and accurate classification of lung nodules plays a crucial role in improving lung cancer prognosis and significantly reducing patient mortality. Delays or inaccuracies in diagnosis often lead to late-stage detection, limiting treatment options and survival rates. To address this challenge, the present study introduces a robust and explainable radiomics-driven framework named Stacked Light Gradient TabNet (SLGT-Net) for reliable differentiation between benign and malignant lung nodules.The proposed framework begins with advanced image preprocessing techniques designed to enhance image quality, normalize intensity variations, and suppress noise artifacts commonly present in medical imaging data. From the preprocessed images, a comprehensive set of handcrafted radiomic features is extracted, capturing morphological properties, texture patterns, and micro-texture characteristics that are closely associated with tumor heterogeneity. These features form an interpretable and clinically meaningful feature space.SLGT-Net leverages a stacking-based ensemble strategy that integrates the complementary strengths of TabNet and Light Gradient Boosting Machine (LightGBM). TabNet employs sequential attention mechanisms to dynamically select the most informative features, enhancing interpretability and reducing redundancy. In parallel, LightGBM efficiently models complex nonlinear relationships within high-dimensional radiomic features. A meta-learner is subsequently employed to fuse the predictions from both models, further improving classification robustness and generalization.To promote clinical trust and transparency, explainable artificial intelligence (XAI) techniques are incorporated through TabNet attention masks and SHapley Additive exPlanations (SHAP) analysis. Experimental evaluation on publicly available datasets demonstrates superior performance, achieving an accuracy of 97.91%, precision of 96.23%, recall of 96.80%, F1-score of 96.51%, and specificity of 96.41%. These results confirm that SLGT-Net provides a reliable, interpretable, and high-performing solution for lung cancer detection and clinical decision support.

Keywords: *Lung cancer detection, Magnetic resonance imaging, Chromated tomography, Explainable artificial intelligence, Handcrafted radiomic features*

1. INTRODUCTION

Lung cancer is a type of cancer that holds second rank in causing death across the world. This affects the normal functions of the lungs. The primary function of the lungs is oxygen exchange and it is affected, and it causes various health issues [1]. Lung cancer is mainly caused due to smoking and the other causes of lung cancer include radon gas exposure, asbestos exposure, genetic factors, lung diseases, air pollution, and a few radiation therapies [2]. It does not exhibit any noticeable symptoms in the early stage. The symptoms may include shortness of breath, persisting coughing, unexplainable weight loss, and chest pain [3]. The imaging techniques used to diagnose lung cancer are computed tomography (CT) and magnetic resonance imaging (MRI) [4]. The radiomic features extracted from these images detect and classify lung cancer. Manual detection of lung cancer is a complicated process and prone to various errors. Highly specialized and trained

clinicians are required to perform the accurate classification of lung cancer [5]. Machine learning (ML) and artificial intelligence (AI) detect and classify lung cancer in recent times to solve the limitations that arise due to human errors.

These algorithms are mainly used to detect lung cancer as benign (non-cancerous) or malignant (abnormal cell growth) [7]. The traditional ML and AI algorithms used to detect and categorize lung cancer exhibit various limitations such as limited feature representation, lack of generalization, poor interpretability, imbalance in data handling, scalability issues, and limited usage of multimodal data [8]. The explainable artificial intelligence (XAI) assists in making transparent, interpretable, and trustworthy predictions [9]. These techniques enhance the conventional ML algorithms by assisting them in solving the limitations. The XAI techniques assist the ML and DL algorithms in validating and refining feature selection, handling bias and class imbalance, performing error analysis, enhancing interpretability, improving generalization, and presenting continuous learning [10]. By utilizing the knowledge obtained from existing literature related to the usage of integrated ML and XAI, this work tends to develop and novel and robust architecture.

1.1 Motivation

Most traditional techniques depend mainly on either the deep features or handcrafted features to exhibit full potential. This develops a gap in attaining high interpretability and accuracy in clinical decision-making. Hence, there is a critical need for a hybrid, robust, and explainable AI model that can process high-dimensional radiomic features, enhance diagnostic precision, and gain clinician trust. A novel hybrid model named Stacked Light Gradient TabNet (SLGT-Net) efficiently integrates the attention-based deep learning (TabNet) and efficient gradient boosting (LightGBM), followed by a meta-learner for final decision-making. Exploring and exploiting the advantages of the models such as ability of the TabNets in choosing the most important features dynamically and the ability of LightGBMs in modelling complex patterns without any loss in explainability utilizing SHAP values and attention masks.

1.2 Research Questions To clearly define the objectives of this research, the following research questions are formulated.

1. Can the integration of TabNet and LightGBM within a stacked ensemble framework improve the classification performance of lung nodules compared with existing standalone machine learning and deep learning approaches?

2. Does the incorporation of dual explainability mechanisms, namely SHAP values and TabNet attention masks, improve the interpretability and clinical reliability of automated lung cancer diagnosis?

3. Can optimized radiomic feature engineering enhance the robustness and generalization capability of the proposed model across heterogeneous CT and MRI datasets?

1.3 Research Hypothesis

Based on the identified research gaps, the study investigates the following hypotheses.

H1: The proposed SLGT-Net framework significantly improves lung nodule classification performance compared with existing machine learning and deep learning methods.

H2: The integration of SHAP-based feature importance and TabNet attention visualization significantly enhances the explainability of model predictions.

H3: The combination of optimized handcrafted radiomic features with stacked ensemble learning improves model robustness and generalization across multiple imaging datasets.

1.4 Novelty

The novelty of this work is presented in the following subsections,

1.4.1Hybrid ensemble of deep learning and gradient boosting

Integration of TabNet (a deep learning model with feature-wise attention) and LightGBM (a gradient boosting machine) is provided by the proposed SLGT-Net model. This hybridization implements both sequential attention-based feature

learning and gradient-boosted decision trees, which was a novel combination in the classification tasks. While utilizing high-dimensional handcrafted features, this fusion improves the robustness and performance.

1.4.2 Stacking-Based Meta-Learning Framework

SLGT-Net implements a meta-learner that stacks the outputs of TabNet and LightGBM, instead of depending on a single predictive output. This stacking architecture efficiently merges the advantages of both based models and understands how to optimize their performance, providing an important enhancement over conventional ensemble or single-model techniques.

1.4.3 Explainability via dual XAI mechanisms

By merging TabNet's attention masks with SHAP analysis from LightGBM, the SLGT-Net presents improved model interpretability. This dual-XAI setup bridges the gap between clinical usability and model transparency, solving the critical issues in implementing AI in healthcare sector.

1.4.4 Comprehensive radiomic feature utilization

The model proposed in this work uses thehandcrafted radiomic features extracted from both MRI and CT scan datasets. When compared to the deep models that targets only the pixel-level patterns, SLGT-Net reduces the value of interpretable radiomic features that are clinically important.

1.4.5Cross-dataset generalizability

The proposed model uses different datasets that includes MRI, CT scans, and COVID-19 lung scans demonstrating high generalization capability over imaging modalities, lung conditions, and nodule types.

1.5 Contribution

The contribution of proposed methodology is presented in the following subsections,

1.5.1 Development of a novel SLGT-Net model

A Stacked Light Gradient TabNet (SLGT-Net) model that merges the attention-based feature selection ability of TabNet with the gradient boosting power of LightGBM, is proposed in this work. This stacked ensemble framework improves the capability to model complex relationships inside the high-dimensional radiomic feature spaces.

1.5.2 Integration of multi-modality lung imaging data

This study integrates and processes lung images from various sources like MRI, CT scans, and COVID-19 lung scans over multiple datasets. This multi-modal data integration ensures the robustness and generalizability of model in identifying various pulmonary diseases, including both benign and malignant nodules, as well as infectious diseases.

1.5.3 Advanced image preprocessing and feature extraction pipeline

A comprehensive preprocessing phase using morphological operations, CLAHE, gamma correction, and bilateral filtering, is implemented in this work. Feature extraction is performed utilizing handcrafted radiomic features like GLCM, LBP, and nodule size descriptors, that preserve important clinical data while reducing noise and redundancy.

1.5.4 XAI with dual interpretability

By merging TabNet's attention masks with LightGBM's SHAP-based global feature importance, the proposed model presents both local and global model interpretability. This ensures transparency in decision-making.

1.5.5 enhanced classification performance through meta-learning

A meta-learner is used to merge the outputs from both TabNet and LightGBM, permitting the final model to attain higher accuracy, sensitivity, and F1-score. This stacking approach efficiently reduces the bias and variance of the model.

1.6 PAPER ORGANIZATION

The subsequent parts of the paper are: Section 2 summarizes prior literature works based on detection and classification. The Proposed methodology is detailed in section 3, The results obtained from the experiments are presented in detail in Section 4, and the paper is finally concluded with Section 5.

2. LITERATURE REVIEW

To detect lung cancer, Wani et al. [11] developed an interpretable DL-based technique utilizing XAI. A novel interpretable hybrid DL-based approach known as DeepXplainer was utilized in this work to detect lung cancer. XGBoost and CNN were the bases of this technique. XGBoost was used to perform class label prediction.

To perform lung cancer classification, Fathalla et al. [12] developed a 3D DL and textual radiomics computational architecture. One of the types of cancer that caused a large number of deaths across the world was lung cancer. A multistage neuro-based computational technique named DETECT-LC was utilized to perform efficient diagnosis and precise staging. The results obtained indicated that the DETECT-LC exhibited efficient diagnosis.

Raza et al. [13] implemented EfficientNet. An increase in life expectancy of the individual affected with lung cancer was possible with the early diagnosis. The main imaging technique used in lung cancer detection was the CT. There was a limitation of higher time consumption in manual CT analysis. Hence, to overcome this limitation, a predictor based on transfer learning (TL) known as Lung-EffNet was utilized in this article. EfficientNet architecture was the base for Lung-EffNet. Experimental outcomes exhibited that the developed model had superior performances.

Kasinathan and Jayakumar [14] employed DL-based approaches to perform lung cancer detection and stage categorization based on the cloud. A hybrid model for CT or positron emission tomography (PET) known as a cloud-based Lung Tumor Detector and Stage Classifier (Cloud-LTDSC) was used in this article to detect and categorize the different stages of lung tumor. The evaluations indicated that the Cloud-LTDSC model exhibited superior performance in detecting and classifying the stages of lung tumors.

To detect various chest diseases, Ibrahim et al. [15] established a multi-classification DL model. Three chest diseases were mistaken during detection and classification, they were COVID-19, lung cancer, and pneumonia. The comparison results indicated that the VGG19 +CNN model exhibited superior performance in the detection and classification of chest diseases.

Mishra et al. [16] established a computationally intelligent healthcare system.An efficient lung cancer detection model was established to merge both computational intelligence and IoHT To classify the normal and lung cancer cases the RF classifier was used. The experimental output exhibited better performance in detecting the risk of lung cancer.

Shafi et al. [17] developed an efficient technique to diagnose from CT images using a support vector network based on DL. Due to the asymptomatic nature of lung cancer, the early diagnosis was a complicated process. This model provided enhanced lung cancer detection performance and effective patient management.

Alshmrani et al. [18] performed multi-class classification from X-rays using DL. It was difficult to accurately detect and differentiate various chest diseases. A DL framework was used to classify these diseases. This model was developed with the integration of VGG19 and three CNN blocks. This model provided better outcomes in terms of accurate and timely diagnosis.

To detect lung cancer, Faruqui et al. [19] introduced a hybrid deep-CNN model. The automatic diagnosis of lung cancer was a complicated task. To perform this, “LungNet” a model based on hybrid DCNN was used in this article. This model was provided with a 22-layered CNN. From the evaluations done, it was observed that the LungNet exhibited better performances.

Ajai and Anitha [20] established a lung cancer classification from CT images with clustering-based lung lobe segmentation and optimization. To efficiently classify lung cancer, a technique named Shuffled Social Sky Optimizer-based Multi-Object Rectified Attention Network (SSSO-based MORAN) was developed. This model exhibited superior performance in the classification.

Mohamed et al. [21] established a DL and ebola optimization search algorithm. To solve the issue of bias combination requirement and choosing optimal weight, a hybrid metaheuristic and CNN algorithm was used. The finest combination of weights and bias was selected by processing the solution vector in the optimization search algorithm (EOSA) to solve the classification issues. The experimental output exhibited that the superior performance in the EOSA-CNN attained optimal values in terms of all the evaluation measures used.

To detect and classify the malignant lung nodules from the CT input in the early stage, Sengodan et al. [22] employed optimal ensemble learning named Multipopulational Neighborhood particle swarm optimized Modified Ensemble Faster Learning (MNPS-MEFL). The enhancement of life chances of lung cancer patients was possible with early detection. Hence, MNPS-MEFL enhanced lung cancer prediction accuracy.

Sreeprada and Vedavathi [23] established a Hybrid DL approach named orthogonal Convolution neural network-support vector machine (OCNN-SVM) model was developed. The OCNN-SVM is the integration of CNN and SVM to detect lung cancer. The evaluations indicated that the developed model exhibited superior performance in terms of lung cancer classification.

Sangeetha et al. [24] developed a multimodal fusion DL neural network (MFDNN) integrated data from various modalities like clinical data, medical imaging, and genomics. The experimental output exhibited timely and accurate detection.

Srivastava et al. [25] implemented a revolutionized DL-based model to detect thedisease early stage. Detection of lung cancer in the early stage was the only potential solution to enhance the life expectancy of affected individuals. To detect lung cancer in the beginning stage, a hybridized faster R-CNN (HFRCNN) was used. This results obtained enhanced detection accuracy during detection process.

Qin et al. [29] reported that integrating radiological, pathological, genomic, and clinical information significantly enhances diagnostic accuracy, although challenges related to data heterogeneity and explainability remain. In response, the proposed SLGT-Net combines optimized radiomic features with an explainable TabNet–LightGBM stacking framework to improve both accuracy and interpretability.

Liu et al. [30] highlighted that future AI systems for lung cancer should incorporate explainability, multimodal learning, and clinical validation to facilitate real-world deployment. Similarly, Allgöwer et al. [31] demonstrated that combining multimodal information with LightGBM and SHAP improves prediction performance and interpretability. Building upon these findings, SLGT-Net integrates TabNet attention with SHAP explanations to provide transparent and reliable lung nodule classification.

Hao et al. [32] introduced a multimodal benchmark for precision lung cancer diagnosis, emphasizing the integration of heterogeneous clinical information for intelligent decision support. Likewise, Desai et al. [33] concluded that multimodal AI improves predictive capability but identified data integration and model transparency as major challenges. Motivated by these observations, SLGT-Net provides a computationally efficient and explainable ensemble framework that combines optimized radiomic feature engineering, TabNet, and LightGBM to achieve accurate and clinically interpretable lung cancer classification.

2.1 Comparison with Existing Studies

Recent advances in artificial intelligence have significantly improved lung cancer classification using computed tomography (CT) images. One representative study, DeepXplainer, employed a convolutional neural network (CNN) combined with explainable deep learning techniques to classify lung cancer. The framework demonstrated superior classification performance while incorporating partial explainability to identify influential image regions. However, the model was evaluated only on CT images, limiting its applicability to multi-modal clinical scenarios. Furthermore, its explainability mechanism primarily focused on visualization rather than providing comprehensive feature-level interpretation, which may reduce clinical transparency in decision-making.

Similarly, DETECT-LC utilized a three-dimensional convolutional neural network (3D-CNN) to exploit volumetric information from CT scans. The use of 3D image representations improved spatial feature extraction and enhanced classification performance compared with conventional two-dimensional approaches. Nevertheless, the framework did not incorporate any explainability mechanism, making its predictions difficult for clinicians to interpret. In addition, the computational complexity associated with 3D-CNN architectures requires substantial processing power and memory resources, thereby limiting practical deployment in healthcare institutions with limited computational infrastructure.

Another recent framework, **Lung-EffNet**, adopted the EfficientNet architecture for automated lung cancer classification from CT images.

EfficientNet achieved excellent classification accuracy by employing compound scaling strategies that balance network depth, width, and image resolution. Despite its strong predictive performance, Lung-EffNet remains a black-box deep learning model with limited interpretability. Consequently, clinicians receive highly accurate predictions without sufficient insight into the reasoning behind the model's decisions, reducing confidence in its clinical adoption.

In contrast, the proposed SLGT-Net addresses several limitations of previous studies by integrating optimized radiomic feature engineering with a stacking ensemble consisting of **TabNet** and LightGBM. Unlike existing methods that rely exclusively on CT imaging, SLGT-Net supports both CT and MRI datasets, thereby improving its applicability across heterogeneous medical imaging environments. Moreover, the proposed framework incorporates dual explainability through TabNet attention masks and SHAP feature attribution, enabling both global and local interpretation of classification decisions. This combination allows clinicians to understand not only which radiomic features influence the prediction but also how the model sequentially allocates attention during the decision-making process.

Compared with DeepXplainer, DETECT-LC, and Lung-EffNet, SLGT-Net provides a more balanced solution by simultaneously emphasizing high classification accuracy, computational efficiency, model transparency, and clinical interpretability. The integration of explainable ensemble learning, optimized radiomic features, and multi-modal image analysis makes the proposed framework particularly suitable for real-world computer-aided diagnosis systems. Consequently, SLGT-Net represents a significant advancement toward trustworthy and clinically deployable artificial intelligence for early lung cancer diagnosis.

2.2 Research Gaps

Detecting and classifying lung cancer is an important measure to be taken to increase the lifespan of patients. The traditional ML techniques used for the detection and classification of lung cancers exhibit various limitations such as low accuracy, reduced generalization, limited scalability, lack of interpretability, class imbalance issues, and inefficient feature extraction. The research gaps formed by these limitations are presented in the following subsections.

2.2.1 Inefficient classification

The unwanted noises in the dataset and the imbalanced dataset in the existing works make the processing complex and reduce the classification accuracy. The methodology proposed in this work contains a robust and efficient preprocessing phase and augmentataion phase to enhance image quality.

2.2.2 Limited integration of data

The integration of data from various models are not performed effectively in many of the exsting techniques. This reduced the performance of the models used and produced poor classification result. In the SLGT-Net, the output from TabNet and LightGBM are integrated with an ensemble learning technique known as stacking.

2.2.3 Insufficient Usage of XAI

The usage of XAI is not explored in the traditional approaches and this study utilizes the explainable AI to improve the transparency, trustworthiness, and clinical applicability of the SLGT-Net model.

3. PROPOSED METHODOLOGY

A comprehensive framework of the proposed methodology is shown in Figure 1. Initially, the collected data are preprocessed using techniques such as the morphological opening, gamma correction, CLAHE, and bilateral Filter to improve the consistency and quality of data. Augmentation techniques are implemented to enhance the generalization and robustness of the model. Then, the handcrafted radiomic features that contain the morphological, textural (GLCM), and micro-textural (LBP) properties are extracted and a feature matrix is formed. A novel Stacked Light Gradient TabNet (SLGT-Net) model is used to classify the features extracted. This model combines the advantages of sequential attention-based learning of TabNet and the gradient-boosting power of LightGBM. Then, the meta-learner refines the features to improve the robustness and predictive accuracy. To ensure the reliability and transparency of the framework by making it appropriate for clinical decision support to employ XAI

techniques such as SHAP analysis and feature importance interpretations.

3.1. Data collection

3.1.1 Lung cancer MRI images:

The lung cancer MRI image dataset contains 1,018 annotated lung MRI images collected from various individuals. To ensure categorization as normal or malignant, four radiologists review and label every single image. In the Lung cancer MRI image dataset (https://www.kaggle.com/datasets/xiaopengzhang12/lung-cancer-mri-images). A standard resolution size of 256×256 pixels is applied to all the images.

Classes:

- Normal - Lung MRI images without the sign of malignancy or visible nodules.
- Malignant- Lung MRI images with nodules identified as cancerous according to the annotation of radiologists.

3.1.2 Chest CT-scan images dataset:

This dataset is generated to design the AI-based models to identify and categorize different kinds of lung cancer (https://www.kaggle.com/datasets/mohamedhanyyy/chest-ctscan-images). Every type indicates real clinical conditions with the common type found in the outer lung known as Adenocarcinoma, the Large cell carcinoma that grows rapidly and is located in various lung areas, and the Squamous cell carcinoma commonly related to smoking and found in central lung regions. This dataset is collected from various sources, cleaned, and labeled to assist DL applications in medical image analysis.

3.1.3 Covid 19 lung CT scans:

The images in this dataset are labeled. 7,495 CT scans are labeled as COVID-19 Positive, this shows that the scans indicate SARS-CoV-2 infection. The other 944 scans are labeled as COVID-19 negative and contain both the normal lungs and lungs affected with conditions other than COVID-19. All the images are stored in PNG format with a resolution of 512×512 pixels. (https://www.kaggle.com/datasets/mehradaria/covid19-lung-ct-scans) was well organized. The binary classification is differentiated as COVID-19 positive and negative.

3.1.4 IQ-OTH/NCCD lung cancer dataset

The images https://www.kaggle.com/datasets/adityamahimkar/iqothnccd-lung-cancer-dataset are collected with a Siemens SOMATOM CT scanner with standardized settings (120KV, 1mm slice thickness). Every scan contains 80-200 slices and is described by oncologists and radiologists. Various patients from central Iraq are included in this dataset which presents valuable data.

3.2. Data pre-processing

Proper image preprocessing is necessary before the images are given as input to the neural networks. This removes the complexities of image structures, distortions, and noise from the input images.

3.2.1 Morphological opening

To eliminate the unwanted small artifacts like tiny objects and noisy spikes from the images the morphological opening is utilized. This process performs two steps such as erosion and dilation utilizing a 5×5 kernel. This process removes unwanted noise background from the MRI and CT images without losing any loss in important dimensions and shapes.

There are two steps in the morphological opening such as erosion and dilation.

3.2.2 Erosion

The erosion process (V) is mathematically presented as follows,

$$V(R) = (R \Theta Y) \quad (1)$$

From the above equation, the input image is indicated as R, the structuring element is represented as Y, and the erosion operation is indicated as Θ.

3.2.3 Dilation

The dilation process is mathematically represented as follows,

$$W(R) = (V(R) \oplus Y) \quad (2)$$

From the above equation, the eroded image is indicated as $V(R)$, and the dilation operation is indicated as $\oplus$.

$$R_{open} = (R \Theta Y) \oplus Y \quad (3)$$

3.2.4 Gamma Correction

The brightness of the images is adjusted with the gamma correction when they are too bright or dark. To enhance the visibility of details in the

images by performing expansion and compression of pixel intensity values, an optimal gamma value of 1.2 is selected.
Gamma correction regulates the image brightness based on the following formula,

$$R_{corrected}(c,b) = X \cdot R(c,b)^{\delta} \quad (4)$$

From the above equation, the pixel intensity value at the position (c,b) is $R(c,b)$, a constant is denoted as X, and the gamma value is indicated as δ.

3.2.5 Contrast Limited Adaptive Histogram Equalization (CLAHE)

By regulating edges and local contrast particularly in the regions containing low contrast, the CLAHE enhances contrast of images. By concentrating on the smaller regions inside the image, the CLAHE solves the issue of oversaturation in the global histogram equalization (HE). This makes the medical image without any loss in the important data. CLAHE splits the image into two parts and implements histogram equalization inside every region. This process is mathematically presented as follows,

A. Local histogram computation for every region I inside the image

$$S_I(r) = \sum_{(c,b)\in I} \tau\left(r - R(c,b)\right) \quad (5)$$

From the above equation, the histogram for the region I is indicated as $S_I(r)$, and the Dirac delta function is indicated as τ.

B. Histogram clipping at a predefined threshold to reduce contrast amplification.

$$S_{I(r)} = \min\left(S_I(r), G\right) \quad (6)$$

From the above equation, the clipping threshold is indicated as G.

C. Histogram normalization for every region and application of mapping to the original pixel intensities.

3.2.6 *Bilateral Filter*

Without any loss in the edges, the bilateral filter smoothes the image. To reduce the impact of Gaussian blur which is a common issue in conventional image filtering techniques, the bilateral filter merges the Euclidean distance and radiometric separation. This technique assists in denoising the image without any loss in the details at the edges.

The bilateral filter smooths an image by taking into account both the pixel value and spatial distance similarity. The filtered output

$$R_{filtered}(c,b) = \frac{1}{D_k} \sum_{(c',b')\in M(c,b)} T_{\varepsilon_h}\left(\|(c,b)-(c',b')\|\right) \cdot T_{\varepsilon_i}\left(R(c,b)-R(c',b')\right) \cdot R(c',b') \quad (7)$$

From the above equation, the neighborhood of the pixel (c,b) is $M(c,b)$, the spatial Gaussian Kernel is T_{ε_h}, the range Gaussian kernel is T_{ε_i}, and a normalization factor is indicated as D_k.

3.3 Data augmentation phase

Rotation, flipping, scaling, translation, contrast or brightness adjustments, and cropping are the commonly used augmentation approaches. Simulation of variations in patient positioning during scanning is assisted by processes such as flipping images vertically or horizontally and rotating images at random angles. To simulate the minor anatomical displacements, translation shifts the images slightly in vertical or horizontal directions. When cropping the region of interest that targets the attention of models on localized features like nodules, zooming or scaling in and out simulates the changes in the scanner zoom levels or field of view. In addition to this, changes in contrast or brightness exhibit various tissue densities and scan settings. Due to the breathing or posture, advanced techniques like elastic transformation implement minute nonlinear transformations that simulate natural anatomical variations.

To ensure that the important features like intensity, shape, and texture of lung nodules remain intact, which are necessary while utilizing handcrafted radiomic features, augmentation techniques need to be selected carefully. The aforementioned transformations assist the model in learning invariant features over different imaging conditions, providing enhancements in accurately differentiating nodules in multiple clinical circumstances.

3.4 Feature Extraction

Lung nodules utilizing handcrafted radiomic features, explainable AI (XAI) plays an important role. The gap between the requirement of transparency in healthcare decision-making and the statistical power of AI is bridged by the explainable AI. The XAI transforms the AI-enabled systems safer, more reliable, and more acceptable for real-world implementation, in the high-stakes environment of cancer diagnosis. The purpose of

feature extraction is to convert every lung nodule into a set of numerical values (features) that can be given as input to the ML models for classification tasks like detecting the nodule types. These features contain the important properties of the lung nodules in terms of parameters such as intensity patterns, texture, and size. A data frame is formed with the extracted features, in this frame every row represents a single lung nodule and every column represents a specific feature.

3.4.1 Data frame preparation

A data frame structure is formed once the features are extracted from the images. Each row represents a single lung nodule and each column represents a particular feature such as contrast, energy, texture descriptors, or nodule size. It is considered an important format as it structures the data in a way that is appropriate for training and validating the ML models. The ability of the model to interpret the relationship between features and class labels efficiently is ensured by organizing the data consistently. This assists in enhancing the classification accuracy of lung abnormality diagnosis.

3.4.2 Nodule Size Calculation (SHAP Feature)

The size of the lung nodule is an important feature that is measured by the count of pixels that form the nodule area in the image. The sum of all pixel values greater than zero over the region of interest (ROI) is the mathematical representation for computing the size of the nodule. The size of the nodule H is mathematically presented as follows,

$$H = \sum_{r=1}^{S}\sum_{q=1}^{D} \amalg\left(R(r,q) > 0\right) \quad (8)$$

From the above equation, the height and width of the image are indicated as S and D. the pixel intensity at position (r,q) is $R(r,q)$, and the indicator function that presents 1 if $R(r,q) > 0$ and otherwise 0. This efficient feature captures the lesion's spatial extent which was the parameter mainly used by the radiologists.

3.4.3 GLCM Features (Texture features)

As the malignant lesions exhibit various complex textures, texture analysis is important for differentiating benign and malignant nodules. The GLCM is calculated to capture these textures. GLCM is the statistical approach that records how the pair of pixel intensities appears in a particular spatial relationship inside an image. Different textual characteristics that measure the appearance of lung nodules are derived from the GLCM. Few Haralick texture features are calculated using this matrix,

3.4.4 Contrast

It computes the intensity across the whole image presented as follows,

$$Contrast = \sum_{r,q} (r-q)^2 K(r,q) \quad (9)$$

3.4.5 Correlation

The joint probability for correlation is presented as follows,

$$Correlation = \frac{\sum_{r,q}(r-\nu_r)(q-\nu_r)K(r,q)}{\varepsilon_r \varepsilon_q} \quad (10)$$

From the above equation, the mean and standard deviations of the marginal distributions are ν and ε.

3.4.6 Energy

It indicates the textural uniformity and is mathematically presented in the following equation,

$$Energy = \sum_{r,q} K(r,q)^2 \quad (11)$$

3.4.7 Homogeneity

It measures the closeness of the distribution of elements and is mathematically presented as,

$$Homogeneity = \sum_{r,q} \frac{K(r,q)}{1+|r-q|} \quad (12)$$

3.4.8 Dissimilarity

It quantizes the variation of gray-level pairs in the GLCM and is calculated as follows,

$$Dissimilarity = \sum_{r,q} |r-q| K(r,q) \quad (13)$$

The aforementioned features provide unique data about the textural structure of the image that is important for detecting malignancy.

3.5 Local Binary pattern (LBP) Features (Micro-texture features)

LBP is used to capture fine-grained local textures, at the same time the GLCM captures broader textural patterns. Based on the center pixel value the LBP functions by thresholding a 3x3 neighborhood of every pixel.

The mathematical representation of a LBP code for a pixel present in the location (c_x, b_x) is,

$$LBP(c_x, b_x) = \sum_{k=0}^{k-1} h(R_k - R_x) \times 2^k \quad (14)$$

From the above equation, $h(c) = 1$ if $c \geq 0$ and 0 otherwise, the center pixel's intensity is indicated as R_x, and the intensities of neighboring pixels are indicated as R_k. When the computation of LBP for all the pixels is completed, a histogram of these LBP codes is produced. From the histogram, statistical measures like LBP energy can be extracted to measure the local texture pattern distribution over the lung nodule area. LBP features are very important, as the cancerous tissues contain a distinctive local texture in comparison with the normal tissues, even though they look the same as on a macro scale.

3.6 Lung Nodule Classification using a novel Stacked Light Gradient TabNet (SLGT-Net) model

Handcrafted radiomic features extracted from the CT and MRI scan images contain properties such as high dimensionality, and sparse, and complex structure, which affects the performance of traditional ML models. To solve this issue, the Stacked Light Gradient TabNet (SLGT-Net) model is proposed based on handcrafted radiomic features obtained from CT and MRI scan images. This SLGT-Net contains the advantages of two models such as TabNet and LightBGM. SLGT-Net captures various feature representations and enhances robustness and predictive accuracy by stacking these two models. To merge the outputs of LightGBM and TabNet, a meta-learner is used, this ensures that the final output is enhanced with the usage of feature extraction based on DL and generalization based on gradient boosting. XAI techniques strengthen the methodologies further, and makes it suitable for clinical decision support. By implementing the attention masks the TabNet presents inherent local interpretability at the same time the LightGBM presents global feature importance insights via approaches like SHAP analysis. The SLGT-Net is highly strengthened by this combination and become suitable for an efficient, interpretable, and robust solution for the lung nodule classification process, assisting in transparent and reliable medical diagnosis.

3.7 Input Feature Representation

A feature vector is constructed for every lung nodule after preprocessing and feature extraction. The input feature vector is presented as follows,

$$C = [c_1, c_2, \cdots, c_w] \in \mathrm{I}^w \quad (15)$$

C represents the feature vector, the total count of handcrafted features obtained from CT and MRI images is indicated as w, and every c_r indicates the value of the $r-th$ feature.

3.8 TabNet Prediction Model

A sequential multistep processing-based single deep learning model is TabNet. This single deep framework learns high-dimensional features by assisting the feature selection process. Every m^{th} step processes a D-dimensional feature vector, where every step presents output to a feature transformer block [26].

$$z[r-1] : N[r] = sparsemax\left(K[r-1] \cdot s_r([z-1])\right) \quad (15)$$

Figure 2: *Architecture of TabNet prediction model*

The architecture of TabNet prediction model is depicted in Figure 2. The equation for attentive transformer and masking procedure is derived below.

$$z[r-1] : N[r] = sparsemax\left(K[r-1] \cdot s_r([z-1])\right) \quad (16)$$

From the above equation, the previous step is indicated as $z[r-1]$ the trainable function, and the priori scale is indicated as sr and $K[r]$.

$$K[r] = \Pi_{q=1}^{r} (\delta - N[q]) \quad (17)$$

From the above equation, the relationship between the enforcement of a feature at single or multiple steps is indicated as δ. The feature is enforced at the given step when $\delta = 1$ and

multiple steps when $\delta = 0$. The attentive transformer chooses the most salient features to generate the transformed feature vector and transfers these features to the learnable mask $N[q]$. The mask provides interpretability and enhances feature selection from the attentive transformer. $Nyq[r]$ Indicates the qth feature of the yth sample.

There is no contribution from the feature, when $Nyq[r] = 0$. Collecting these masks at every phase generates final decision. Every mask scores features that assist in the decision of the model and every step generates a mask.

3.9 LightGBM prediction model

An effective and scalable gradient-boosting architecture that generates decision trees iteratively is the LightGBM [27]. The errors generated by the previous trees are corrected by the new trees and the weighted sum of all trees is the final prediction. To reduce the loss function by regulating the weight of every tree iteratively, LightGBM utilizes gradient boosting. It is optimized when high-dimensional and large datasets are used. The LightGBM sequentially develops decision trees, where the prediction of every tree is integrated into the final result utilizing a weight. The formula for prediction is presented in the following equation,

$$\hat{b} = \sum_{r=1}^{N} \beta_r G_r(C) \quad (18)$$

From the above equation, the count of trees is indicated as N the prediction of the r^{th} tree $G_r(C)$, and the weight of the r^{th} tree is indicated as β_r.

Every tree in LightBGM is trained in a way that minimizes the error produced by the previous trees utilizing the gradient of the loss function that permits LightBGM to attain high predictive accuracy.

3.10 Stacking the outputs

When the individual models such as TabNet and LightGBM processed the handcrafted feature vector c, every model generates its prediction score. The predictions are indicated as follows,

$$\hat{b}TabNet = uTabNet(c), the\ probability\ output\ from\ the\ TabNet\ model \quad (19)$$

$$\hat{b}LGBM = uLGBM(c), the\ probability\ output\ from\ the\ LightGBM\ model \quad (20)$$

Instead of utilizing these outputs individually, they are merged into a simple feature vector by integration. This integrated feature vector X is presented as follows,

$$a = \left[\hat{b}TabNet, \hat{b}LGBM\right] \in I^2 \quad (21)$$

From the above equation, a two-dimensional feature vector is indicated as a every dimension indicates the probability score produced by one of the two models. This stacked feature a efficiently merges the predictive insights obtained from both the LightGBM and TabNet, collecting multiple perspectives of the feature space given as input.

3.11 Meta-Learner Prediction

The next step is an important one that includes utilizing a meta-learner to perform the final prediction according to the stacked outputs. An additional model trained on the top of outputs of the base model to learn the advantage of merging their predictions to perform accurate final classification [28].

A function $t(\cdot)$ denotes the meta-learner. By considering a as input, it generates the final predicted probability $\hat{b}final$ and is mathematically presented as,

$$\hat{b}final = t(a) \quad (22)$$

By expanding a:

$$\hat{b}final = t\left(\hat{b}TabNet, \hat{b}LGBM\right) \quad (23)$$

From the above equation, the final probability score is indicated as $\hat{b}final \in [0,1]$. This stacking technique assists in enhancing performance by minimizing the biases or blind spots of individual models and produces a robust and stronger decision-making mechanism. Figure 3 shows the layer architecture of proposed model.

3.12 XAI Module for Model Transparency

The XAI module is integrated with the proposed SLGT-Net model to ensure trust, transparency, as well as clinical reliability to predict lung nodules. It is necessary to classify the prediction outcome, which is interpretable both at global and local levels. The proposed SLGT-Net model uses a dual-level explainability mechanism that combines TabNet attention masks for local interpretability and SHAP analysis from LightGBM for global feature significance.

Local Explanation using TabNet Attention Masks*:* At every decision step, TabNet generates a sparse attention mask $m^{(t)}$ that highlights radiomic features. The mask is computed as,

$$m^{(t)} = Sparsemax(P^{(t)} \cdot a(X)) \quad (24)$$

From the above equation, the prior scale controlling feature reuse is $P^{(t)}$, the attentive transformer output is $a(X)$, and $Sparsemax$ enforces the rate of sparsity. These masks provide a sample-wise interpretability to identify different features, such as nodule size, GLCM contrast, and LBP energy contributed most to a specific benign or malignant decision.

Global Explanation using SHAP with LightGBM*:* A SHAP is applied to the LightGBM predictions to compute the behavior of proposed SLGT-Net model. The following expression is computed as,

$$\phi i = \sum_{S \subseteq F,\ \{i\}} \frac{|S|!(|F|-|S|-1)!}{|F|!}[f(S \cup \{i\}) - f(S)] \quad (25)$$

From the above equation, F indicates the feature set and $f(S)$ is the feature subset. SHAP explains the contribution of each radiomic feature by distributing prediction among features.

4. EXPERIMENTAL RESULTS

The results obtained from the experiments done on the techniques used in this works are presented with tables, graphical representations, and confusion matrices in this section. This section also presents the experimental setup used and parameter settings done.

4.1. Experimental setup

Python 3.10 programming language is used to implement the classification of lung diseases. The experiments are conducted on a hardware setup with an Intel (R) Celeron (R) N4020 CPU @ 1.10GHz, operating on a 64-bit operating system utilizing a processor architecture based on X64. This system also contains a RAM of 4.00 GB.

4.2. Parameter settings

The hyperparameters used for the optimal functioning of SLGT-Net is depicted in Table 1. These hyperparameters assist the SLGT-Net model in attaining the higher lung cancer classification performance.

4.3. Evaluation measures

In this section, true positive is indicated as $TruPos$, true negative is deoted as $TruNeg$, false positive is represented as $FalsPos$, and false negative is presented as $FalsNeg$.

- **Accuracy**

Accuracy computes the correctly classified classes using the following formula,

$$Accuracy = \frac{TruPos + TruNeg}{TruPos + TruNeg + FalsPos + FalsNeg} \quad (26)$$

- **Precision**

Precision computes the positive classes predicted correctly from all classes. The mathematical representation of precision is presented as follows,

$$\Pr ecision = \frac{TruPos}{TruPos + FalsPos} \quad (27)$$

- **Recall**

Recall computes actual positive classes that are predicted as positive.

$$\mathrm{Re}call = \frac{TruPos}{TruPos + FalsNeg} \quad (28)$$

- **F1-score**

The F1-score (mean of precision and recall) is computed based on the following equation,

$$F1 - score = 2\frac{\Pr ecision * \mathrm{Re}call}{\Pr ecision + \mathrm{Re}call} \quad (29)$$

- **Specificity**

The amount of actual negative classes correctly predicted as negative is referred to as specificity. It is calculated as follows,

$$Specificity = \frac{TruNeg}{TruNeg + FalsPos} \quad (30)$$

- **False Positive Rate (FPR)**

FPR computes actual negative cases classified incorrectly as positive. The computation of FPR is done based on the following equation,

$$FPR = \frac{FalsPos}{FalsPos + TruNeg} \quad (31)$$

4 False Negative Rate (FNR)

It is the metric that indicates how often a model misses the actual positive cases. It is mathematically presented as follows,

$$FNR = \frac{FlasNeg}{FalsNeg + TruPos} \quad (32)$$

5 False Detection Rate (FDR)

It is the amount of predicted positive classes that are actually negative. It is calculated using the following formula,

$$FDR = \frac{FalsPos}{TruPos + FalsPos} \quad (33)$$

6 Negative Predicted Value (NPV)

It is the amount of correctly predicted negative classes from all classes predicted as negative. It is mathematically represented as follows,

$$NPV = \frac{TruNeg}{TruNeg + FalsNeg} \quad (34)$$

7 Matthews Correlation Coefficient (MCC)

MCC validate the classification quality of the ML models which is computed using the following equation,

$$MCC = \frac{(TruPos \times TruNeg) - (FalsPos \times FalsNeg)}{\sqrt{(TruPos + FalsPos)(TruPos + FalsNeg)(TruNeg + FalsPos)(TruNeg + FalsNeg)}} \quad (35)$$

4.4. Visual representation of preprocessing and augmentation phases

Table 2 presents the visual representation of data preprocessing phase and Table 3 presents the visual representation of the data augmentation phase.

4.5. Performance analysis

The analysis of performances attained by the proposed SLGT-Net model while evaluating with four different datasets.

8 Confusion matrix

The confusion matrices of the multi-class classification modelfrom four different datasets are shown in Figure 4 (a) Lung cancer MRI images (b) Chest CT-scan images dataset (c) Covid 19 lung CT scans and (d) IQ-OTH/NCCD lung cancer dataset. The higher values in the diagonal indicate the strong classification performance of the model. Hence, these confusion matrices indicate that the SLGT-Net model exhibits superior classification performances.

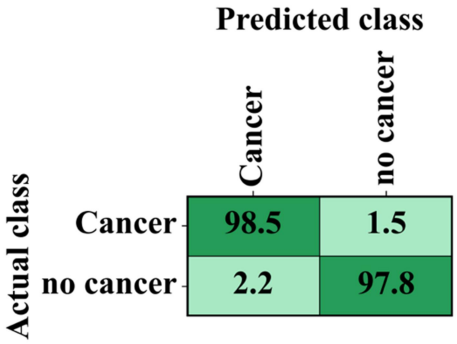

(a)

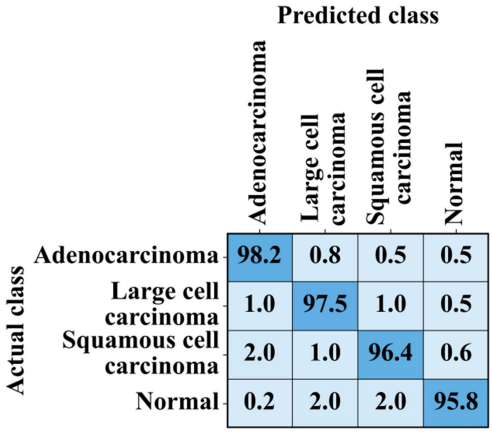

(b)

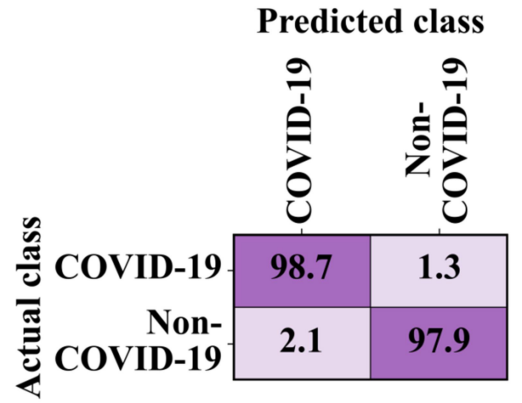

(c)

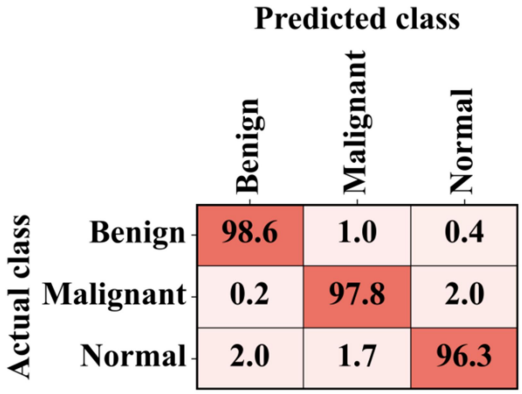

(d)

Figure 4: *Confusion matrix (a) Lung cancer MRI images (b) Chest CT-scan images dataset (c) Covid 19 lung CT scans (d) IQ-OTH/NCCD lung cancer dataset*

Figure 5 (a) shows the analysis of training and testing accuracy attained by the SLGT-Net model. The training accuracy is noted while training the algorithm and testing accuracy is noted while testing the algorithm. The analysis of loss attained by the SLGT-Net model is shown in Figure 5 (b). Both the loss curves gradually decrease gradually and the values indicate the superiority of SLGT-Net model during classifcation processes.

Table 4 provides analysis of various radiomic features for single lung nodule classification. Features such as nodule size, GLCM contrast, GLCM energy, GLCM homogeneity, LBP energy, entropy, and texture variance are analyzed with respect to different decision steps and the mean attention score is computed. The nodule size with high attention score indicates that physical size and texture irregularity are the most influential factors in individual predictions.

Table 5 presents the global importance of radiomic features using SHAP values from LightGBM. Nodule size has the highest SHAP value, proving it is the strongest predictor of malignancy across the dataset. LBP-based features and texture variance contributes moderately to low values.

4.6. Comparative analysis

In this section, the performance of the proposed SLGT-Net model is compared with the existing techniques such as DeepXplainer [11], DETECT-LC [12], Lung-EffNet [13], OCNN-SVM [23], MFDNN [24], and HFRCNN [25] in terms of the evaluation measures used. For this comparison, the mean values of the performance of techniques used on the four different datasets are used.

Figure 6 (a) presents the accuracy analysis for SLGT-Net and existing models. From the graph, it is observed that the SLGT-Net model attained 97.91% accuracy which demonstrated the superiority. The precision comparison used in this work is shown in Figure 6 (b). The SLGT-Net model attains a higher precision value of 96.23% and exhibits its efficiency. Figure 6 (c) shows recall analysis with 96.80% and showed its effectiveness.

Figure 7 (a) shows specificity comparison for SLGT-Net and existing models. The orange color line indicates the different specificity values achieved by the methods. The SLGT-Net attained the higher specificity value of 96.41% and exhibited its effectiveness. The comparison of F1-score values attained by the methods used in this work is shown in Figure 7 (b). The comparison indicates the proposed SLGT-Net attained the high F1-score value of 96.51%. In Figure 7 (c), the lower FPR value indicates the higher performance of the model. From this graph, the proposed SLGT-Net model attained a lower FPR value of 3.58% and showed its effectiveness.

Figure 8 (a) compares the FNR result analysis attained by the SLGT-Net and existing models. The lower FNR denotes the higher performance of the model. The bars indicate the FNR values achieved by the models used. This graph indicates that the proposed SLGT-Net model attained the lowest FNR value of 3.19% and showed its effectiveness. In Figure 8 (b), the lower FDR values indicate the higher performance of the model. The proposed SLGT-Net model attains a

lower FDR value of 5.67% and exhibits its efficiency. In Figure 8 (c), the proposed SLGT-Net model achieved the highest NPV value of 96.95% and exhibited its efficiency.

The comparative analysis of MCC for SLGT-Net and existing models is depicted in figure 9. The higher MCC value provides better performances which indicates the SLGT-Net model with enhanced classification performances. From this graph, it is observed that the SLGT-Net attained the higher MCC value of 0.96 and exhibited its effectiveness. This shows that SLGT-Net model is more reliable and balanced than the existing methods.

4.7 Ablation Study

Table 6 depicts the ablation results to determine the effectiveness of the proposed model. This section evaluates the contribution of different stages systematically. In the absence of any of the elements, a significant reduction in the performance of the proposed SLGT-Net model occurs. This table shows the contribution of every element in improving the accuracy of detection and the SLGT-Net model attained enhanced performances.

4.8 Statistical analysis

4.8.1McNamar's statistical test analysis

McNamar's test is conducted to statistically evaluate the performances of SLGT-Net model in comparison with base models. The P-value for every base model is presented in Table 7. From the table, SLGT-Net contains a P-value of 0.0147, DeepXplainer with a P-value of 0.0235, DETECT-LC with a P-value of 0.0362, Lung-EffNet contains the P-value of 0.0388, OCNN-SVM contains the P-value of 0.0421, MFDNN contains the P-value of 0.0443, and HFRCNN contains the P-value of 0.0497. The null hypothesis for all models is rejected when the P-values attained are all less than the threshold of 0.05. The low P-values for MFDNN and HFRCNN indicate highly important differences, at the same time slightly higher P-value for SLGT-Net assists in significant performance enhancement. These results indicate the efficiency of the proposed ensemble technique in implementing the complementary strengths of the base models providing superior performance.

5. CONCLUSION

The present study introduced **SLGT-Net**, an explainable stacked ensemble framework for automated lung nodule classification using CT and MRI images. The proposed framework integrates optimized radiomic feature extraction, TabNet, LightGBM, stacking ensemble learning, and dual explainability through SHAP analysis and TabNet attention visualization. The primary objective of this research was to develop a clinically reliable artificial intelligence model that not only achieves high classification accuracy but also provides transparent and interpretable decision-making suitable for computer-aided diagnosis. Unlike many existing machine learning and deep learning approaches that emphasize predictive performance alone, SLGT-Net was designed to balance diagnostic accuracy, computational efficiency, and explainability, thereby addressing several important limitations identified in previous studies.

Extensive experimental evaluation demonstrated that the proposed framework consistently outperformed several conventional machine learning and deep learning methods across multiple evaluation metrics. The achieved classification accuracy of **97.91%**, together with high precision, recall, specificity, and F1-score, indicates the robustness and effectiveness of the proposed architecture for distinguishing benign and malignant pulmonary nodules. The incorporation of optimized radiomic features significantly improved feature representation, while the stacked combination of TabNet and LightGBM effectively captured complementary decision boundaries. The statistical validation and ablation analysis further confirmed that each component of the proposed framework contributes meaningfully to the overall predictive performance and stability of the model.

One of the principal contributions of this research is the integration of explainable artificial intelligence into the lung cancer classification pipeline. Although recent deep learning models have demonstrated impressive predictive capabilities, many remain difficult to interpret because of their black-box decision-making processes. In contrast, the proposed SLGT-Net combines SHAP feature attribution with TabNet attention visualization to provide both global and local explanations of model predictions. This dual explainability enables clinicians to identify the radiomic features influencing each prediction while simultaneously understanding how the model allocates attention during classification. Consequently, the proposed framework enhances transparency, improves physician confidence, and increases the potential for clinical acceptance of artificial intelligence-assisted diagnostic systems.

The research questions formulated at the beginning of this study have been successfully

addressed through comprehensive experimental analysis. The results confirm that integrating TabNet and LightGBM within a stacked ensemble framework substantially improves classification performance compared with individual classifiers. Furthermore, the explainability mechanisms incorporated into SLGT-Net provide meaningful clinical interpretation without compromising predictive accuracy. The experimental findings also support the hypothesis that optimized radiomic feature engineering contributes to improved robustness and generalization across heterogeneous imaging datasets. Collectively, these findings demonstrate that the proposed framework effectively satisfies the research objectives while contributing to the growing field of explainable artificial intelligence for medical image analysis.

Despite the encouraging results, several limitations should be acknowledged. The experimental validation was performed using publicly available datasets, and therefore external validation using large multi-center clinical datasets remains necessary before widespread clinical deployment. Additionally, the present investigation focused on binary classification of pulmonary nodules; future research should extend the framework to multi-class classification involving different pathological subtypes of lung cancer. Although handcrafted radiomic features provided strong interpretability, combining these features with deep representation learning may further improve diagnostic performance. Prospective clinical studies involving radiologists and oncologists will also be valuable for assessing the practical utility of the proposed explainability mechanisms in routine healthcare environments.

Future research should concentrate on extending SLGT-Net toward three-dimensional volumetric imaging, multimodal data fusion incorporating PET-CT and histopathological information, federated learning for privacy-preserving collaborative diagnosis, transformer-based architectures, and foundation models for medical imaging. Additional investigation into uncertainty estimation, continual learning, and clinician-in-the-loop artificial intelligence may further improve the reliability and adaptability of computer-aided diagnosis systems. Moreover, integrating the proposed framework into hospital information systems and picture archiving and communication systems (PACS) could facilitate real-time clinical deployment and enable seamless interaction between artificial intelligence models and healthcare professionals.

In conclusion, **SLGT-Net** represents a significant advancement in explainable machine learning for lung cancer diagnosis by successfully integrating accurate classification, efficient ensemble learning, optimized radiomic feature engineering, and clinically meaningful explainability within a unified framework. The proposed methodology not only achieves excellent predictive performance but also addresses the critical requirement for transparency in healthcare artificial intelligence. These characteristics position SLGT-Net as a promising decision-support tool capable of assisting radiologists in early lung cancer diagnosis while promoting trustworthy, interpretable, and clinically responsible adoption of artificial intelligence in modern medical practice.

REFERENCES:

[1] Atmakuru, A., Chakraborty, S., Faust, O., Salvi, M., Barua, P.D., Molinari, F., Acharya, U.R. and Homaira, N., 2024. Deep learning in radiology for lung cancer diagnostics: A systematic review of classification, segmentation, and predictive modeling techniques. *Expert Systems with Applications*, p.124665.

[2] Ren, Z., Zhang, Y. and Wang, S., 2022. A hybrid framework for lung cancer classification. *Electronics*, *11*(10), p.1614.

[3]Agarwal, A. and Patni, K., 2021, July. Lung cancer detection and classification based on alexnet CNN. In *2021 6th international conference on communication and electronics systems (ICCES)* (pp. 1390-1397). IEEE.

[4] Anagnostopoulos, A.K., Gaitanis, A., Gkiozos, I., Athanasiadis, E.I., Chatziioannou, S.N., Syrigos, K.N., Thanos, D., Chatziioannou, A.N. and Papanikolaou, N., 2022. Radiomics/radiogenomics in lung cancer: basic principles and initial clinical results. *Cancers*, *14*(7), p.1657.

[5] Usharani, C., Revathi, B., Selvapandian, A. and Elizabeth, S.K., 2024. Lung Cancer Detection in CT Images Using Deep Learning Techniques: A Survey Review. *EAI Endorsed Transactions on Pervasive Health & Technology*, *10*(1).

[6] Shimazaki, A., Ueda, D., Choppin, A., Yamamoto, A., Honjo, T., Shimahara, Y. and Miki, Y., 2022. Deep learning-based algorithm for lung cancer detection on chest

radiographs using the segmentation method. *Scientific Reports*, *12*(1), p.727.

[7] Nooreldeen, R. and Bach, H., 2021. Current and future development in lung cancer diagnosis. *International journal of molecular sciences*, *22*(16), p.8661.

[8] de Margerie-Mellon, C. and Chassagnon, G., 2023. Artificial intelligence: A critical review of applications for lung nodule and lung cancer. *Diagnostic and interventional imaging*, *104*(1), pp.11-17.

[9]Al-Huseiny, M.S. and Sajit, A.S., 2021. Transfer learning with GoogLeNet for detection of lung cancer. *Indonesian Journal of Electrical Engineering and computer science*, *22*(2), pp.1078-1086.

[10] Nahiduzzaman, M., Abdulrazak, L.F., Ayari, M.A., Khandakar, A. and Islam, S.R., 2024. A novel framework for lung cancer classification using lightweight convolutional neural networks and ridge extreme learning machine model with SHapley Additive exPlanations (SHAP). *Expert Systems with Applications*, *248*, p.123392.

[11] Wani, N.A., Kumar, R. and Bedi, J., 2024. DeepXplainer: An interpretable deep learning based approach for lung cancer detection using explainable artificial intelligence. *Computer Methods and Programs in Biomedicine*, *243*, p.107879.

[12] Fathalla, K.M., Youssef, S.M. and Mohammed, N., 2022. DETECT-LC: A 3D deep learning and textural radiomics computational model for lung cancer staging and tumor phenotyping based on computed tomography volumes. *Applied Sciences*, *12*(13), p.6318.

[13] Raza, R., Zulfiqar, F., Khan, M.O., Arif, M., Alvi, A., Iftikhar, M.A. and Alam, T., 2023. Lung-EffNet: Lung cancer classification using EfficientNet from CT-scan images. *Engineering Applications of Artificial Intelligence*, *126*, p.106902.

[14] Kasinathan, G. and Jayakumar, S., 2022. Cloud-Based Lung Tumor Detection and Stage Classification Using Deep Learning Techniques. *Biomed research international*, *2022*(1), p.4185835.

[15] Ibrahim, D.M., Elshennawy, N.M. and Sarhan, A.M., 2021. Deep-chest: Multi-classification deep learning model for diagnosing COVID-19, pneumonia, and lung cancer chest diseases. *Computers in biology and medicine*, *132*, p.104348.

[16] Mishra, S., Thakkar, H.K., Mallick, P.K., Tiwari, P. and Alamri, A., 2021. A sustainable IoHT based computationally intelligent healthcare monitoring system for lung cancer risk detection. *Sustainable Cities and Society*, *72*, p.103079.

[17] Shafi, I., Din, S., Khan, A., Díez, I.D.L.T., Casanova, R.D.J.P., Pifarre, K.T. and Ashraf, I., 2022. An effective method for lung cancer diagnosis from ct scan using deep learning-based support vector network. *Cancers*, *14*(21), p.5457.

[18] Alshmrani, G.M.M., Ni, Q., Jiang, R., Pervaiz, H. and Elshennawy, N.M., 2023. A deep learning architecture for multi-class lung diseases classification using chest X-ray (CXR) images. *Alexandria Engineering Journal*, *64*, pp.923-935.

[19] Faruqui, N., Yousuf, M.A., Whaiduzzaman, M., Azad, A.K.M., Barros, A. and Moni, M.A., 2021. LungNet: A hybrid deep-CNN model for lung cancer diagnosis using CT and wearable sensor-based medical IoT data. *Computers in Biology and Medicine*, *139*, p.104961.

[20] Ajai, A.K. and Anitha, A., 2022. Clustering based lung lobe segmentation and optimization based lung cancer classification using CT images. *Biomedical Signal Processing and Control*, *78*, p.103986.

[21] Mohamed, T.I., Oyelade, O.N. and Ezugwu, A.E., 2023. Automatic detection and classification of lung cancer CT scans based on deep learning and ebola optimization search algorithm. *Plos one*, *18*(8), p.e0285796.

[22] Sengodan, P., Srinivasan, K., Pichamuthu, R. and Matheswaran, S., 2023. Early detection and classification of malignant lung nodules from CT images: An optimal ensemble learning. *Expert Systems with Applications*, *229*, p.120361.

[23] Sreeprada, V. and Vedavathi, K., 2023. Lung Cancer Detection from X-Ray Images using Hybrid Deep Learning Technique. *Procedia Computer Science*, *230*, pp.467-474.

[24] Sangeetha, S.K.B., Mathivanan, S.K., Karthikeyan, P., Rajadurai, H., Shivahare, B.D., Mallik, S. and Qin, H.,2024. An enhanced multimodal fusion deep learning neural network for lung cancer classification. *Systems and Soft Computing*, *6*, p.200068.

[25] Srivastava, D., Srivastava, S.K., Khan, S.B., Singh, H.R., Maakar, S.K., Agarwal, A.K.,

Malibari, A.A. and Albalawi, E., 2023. Early Detection of Lung Nodules Using a Revolutionized Deep Learning Model. *Diagnostics*, *13*(22), p.3485.

[26] Shah, C., Du, Q. and Xu, Y., 2022. Enhanced TabNet: Attentive interpretable tabular learning for hyperspectral image classification. *Remote Sensing*, *14*(3), p.716.

[27] Hamed, E.A.R., Salem, M.A.M., Badr, N.L. and Tolba, M.F., 2023. An efficient combination of convolutional neural network and LightGBM algorithm for lung cancer histopathology classification. *Diagnostics*, *13*(15), p.2469.

[28] Chen, H. and Bajorath, J., 2023. Meta-learning for transformer-based prediction of potent compounds. *Scientific Reports*, *13*(1), p.16145.

[29] Y. Qin, S. Wang, D. Wu, Y. Fei, W. Ding, Q. Wang, R. Guan, and X. Liang, "A Review of Deep Learning-Based Multimodal Data Integration of Lung Cancer," Clinical and Experimental Medicine, vol. 26, Art. no. 275, 2026, doi: 10.1007/s10238-026-02184-6.

[30] N. Liu, G. Han, Q. Gu, Y. Zhang, and M. Chen, "A New Era of Precision Diagnosis and Treatment for Lung Cancer: Artificial Intelligence-Driven Multimodal Data Integration and Clinical Applications," *Cell Death & Disease*, vol. 17, 2026

[31] A. Allgöwer, M. Johansson, A. Hallqvist, J. Andersson, Å. Johnsson, I. Häggström, and J. Alvén, "Data-Efficient and Explainable Multimodal Survival Prediction in NSCLC Using Deep Image Embeddings, Clinical Variables, and Gradient-Boosted Trees," *Diagnostics*, vol. 16, no. 12, Art. 1941, 2026, doi: 10.3390/diagnostics16121941

[32] F. Hao *et al.*, "LungCURE: Benchmarking Multimodal Real-World Clinical Reasoning for Precision Lung Cancer Diagnosis and Treatment," *arXiv preprint* arXiv:2604.06925, 2026.

[33] A. Desai *et al.*, "Artificial Intelligence and Machine Learning in Non-Small Cell Lung Cancer: The Current State of the Science on Multi-Omic Applications," *BMC Medical Research Methodology*, vol. 26, Art. no. 86, 2026.

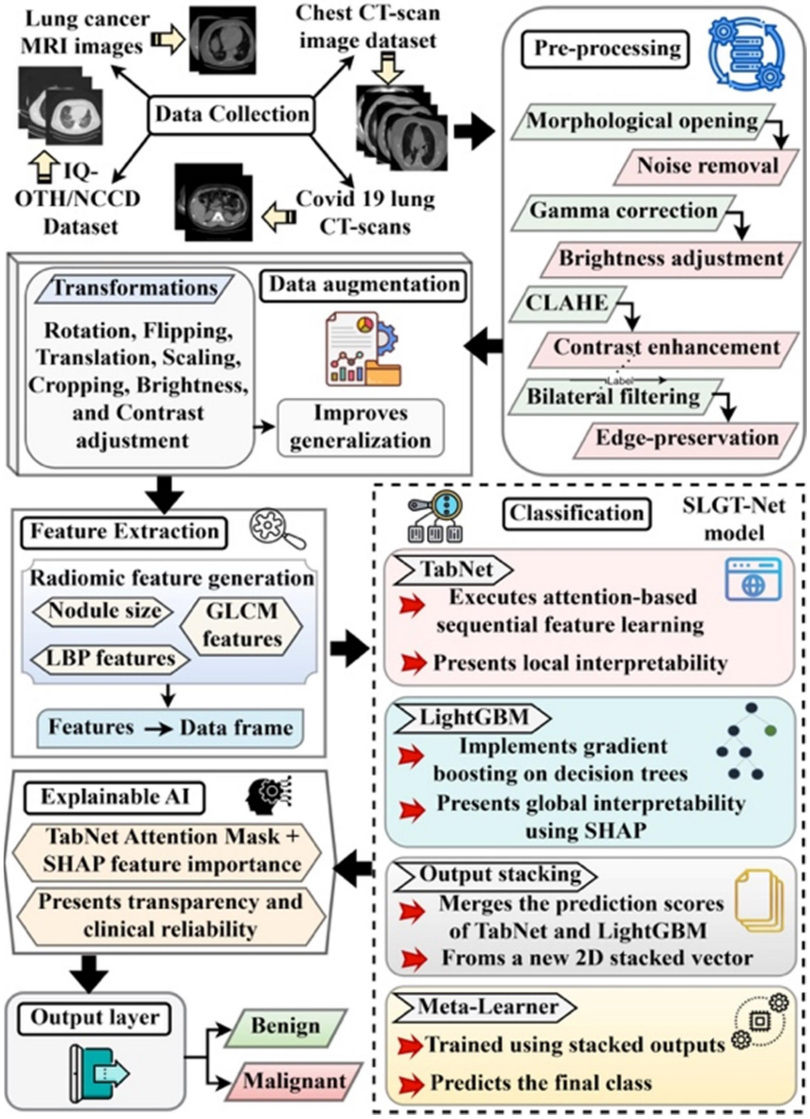

Figure 1: Conceptual proposed workflow

Table 1: *Parameters used for the optimal functioning of SLGT-Net model*

Component	Parameter	Description	Optimal value
TabNet	Batch size	Training batch size	512
	Gamma	Relaxation parameter for attention	1.5
	n_d,n_a	Dimensions of Feature and Attention Transformer	64
	Lambda_sparse	Sparsity regularization coefficient	0.0001
	n_steps	Count of decision steps	5
LightGBM	Min_child_samples	Minimum data per leaf	20
	Num_leaves	Maximum leaves per tree	31
	Max_epochs	Maximum Training epochs	100
	Max_depth	Maximum depth of the tree	7
	Batch_size	Size of the training batch	512
Meta-Learner	Regularization ©	Inverse regularization strength	1.0
	Model type	Algorithm utilized for the final decision	Logistic Regression

`

Table 2: *Visual representation of data preprocessing phase*

Input image	Erosion	Dilation	Gamma correction	CLAHE	Bilateral Filter
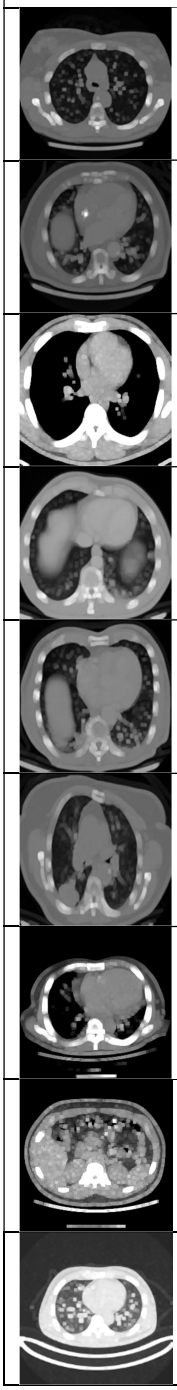					

Table 3: *Visual representation of data augmentation phase*

Input	Data augmentation phase						
	Rotation	Flipping	Translation	Scaling	Cropping	Contrast	Brightness
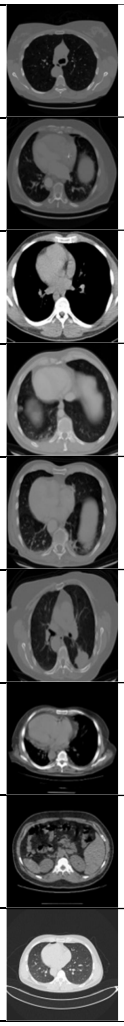	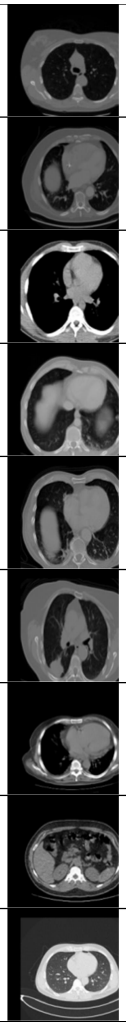	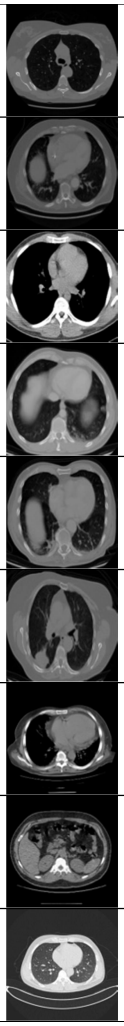	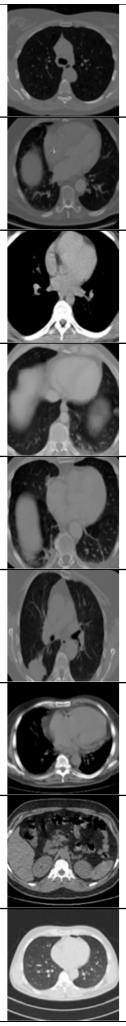	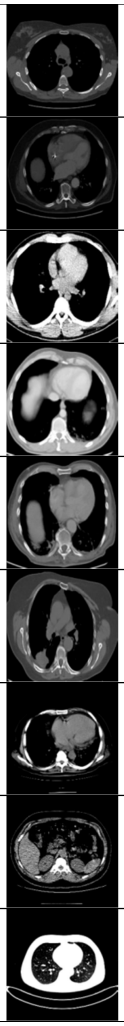	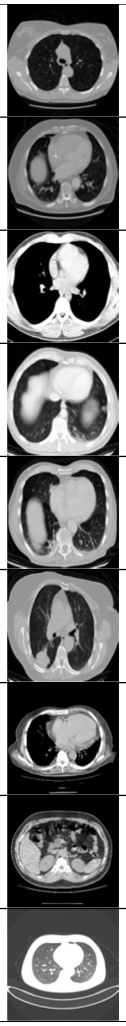	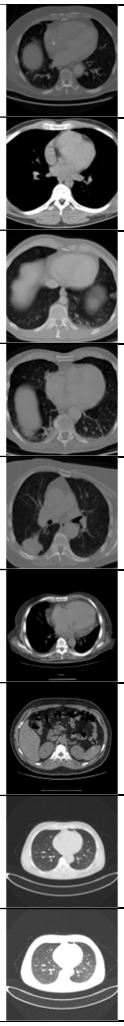	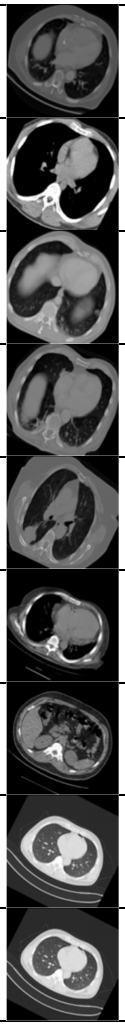

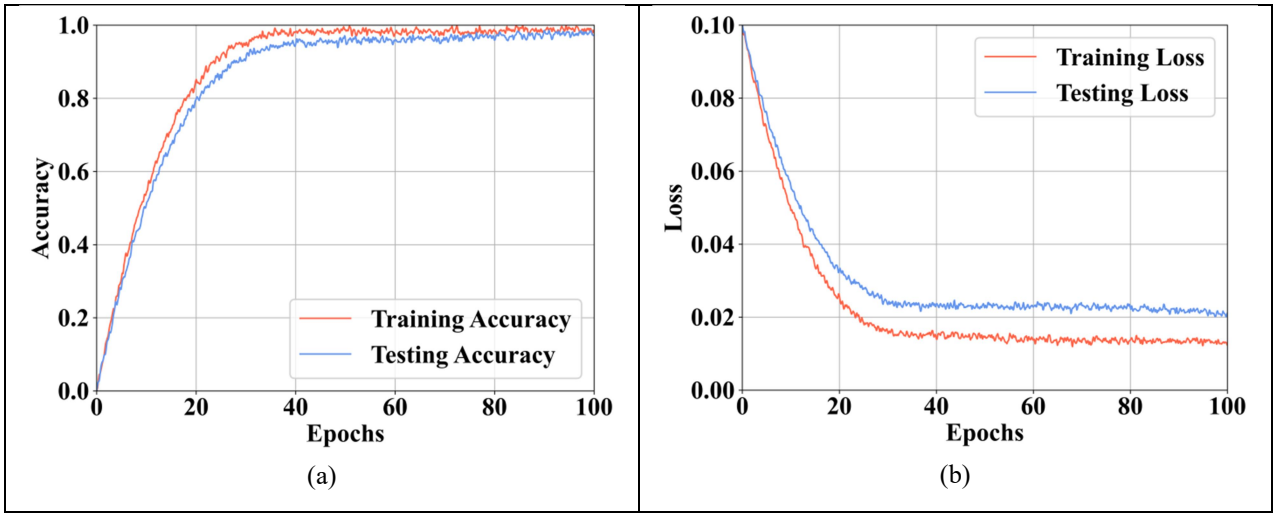

Figure 5: *Testing and Training analysis (a) accuracy (b) loss*

Table 4: *TabNet Attention Mask score analysis for various Radiomic features representing the local explainability*

Radiomic Feature	Decision Step-1	Decision Step-2	Decision Step-3	Decision Step-4	Decision Step-5	Mean Attention Score
Nodule Size	0.92	0.90	0.88	0.93	0.91	0.908
GLCM Contrast	0.85	0.82	0.87	0.86	0.84	0.848
GLCM Energy	0.79	0.81	0.78	0.80	0.82	0.800
GLCM Homogeneity	0.74	0.72	0.70	0.73	0.71	0.720
LBP Energy	0.68	0.70	0.67	0.69	0.66	0.680
LBP Entropy	0.61	0.63	0.60	0.62	0.59	0.610
Texture Variance	0.55	0.57	0.56	0.58	0.54	0.560

Table 5: *Analysis based on Global SHAP feature importance from LightGBM*

Rank	Radiomic Feature	Mean SHAP Value	Contribution Level
1	Nodule Size	0.412	Very High
2	GLCM Contrast	0.356	Very High
3	GLCM Energy	0.291	High
4	GLCM Homogeneity	0.244	High
5	LBP Energy	0.198	Moderate
6	LBP Entropy	0.162	Moderate
7	Texture Variance	0.118	Low

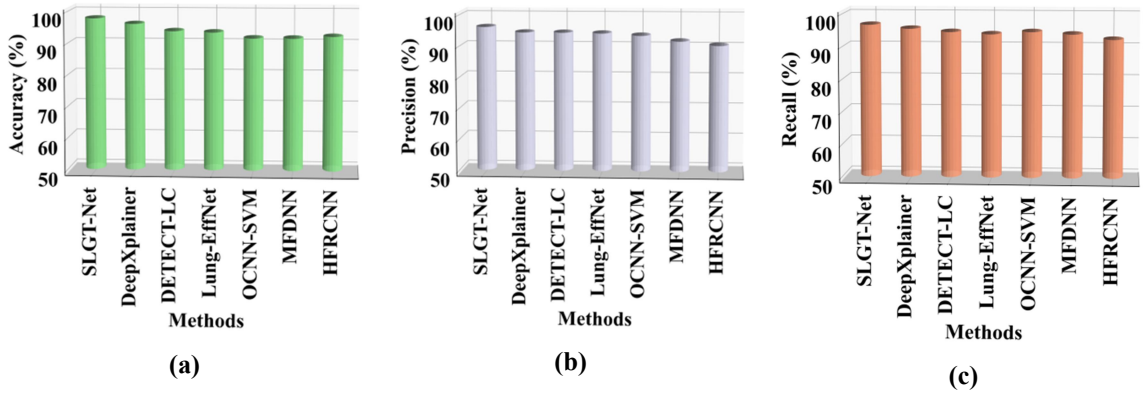

Figure 6: *Comparative analysis of (a) accuracy (b) precision (C) recall*

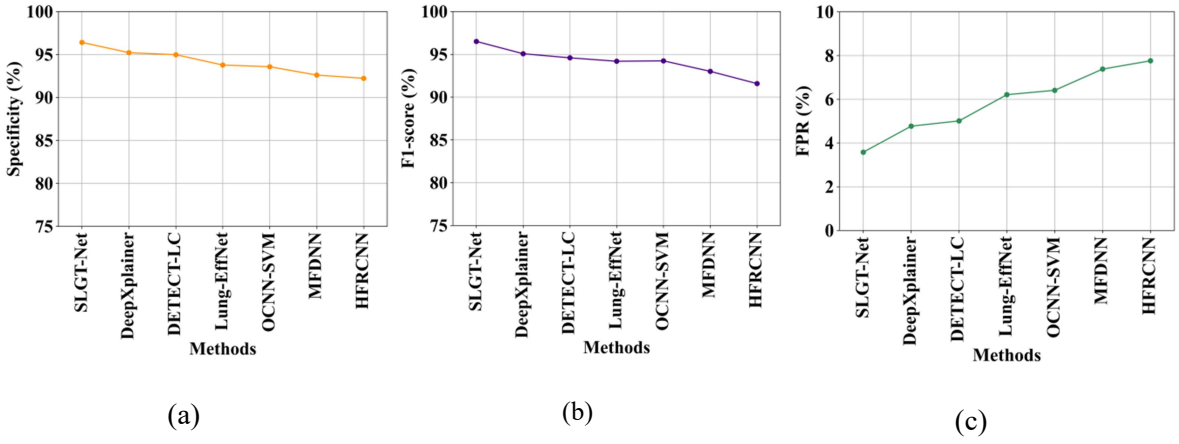

Figure 7: *Comparative analysis of (a) specificity (b) F1-score (c) FPR*

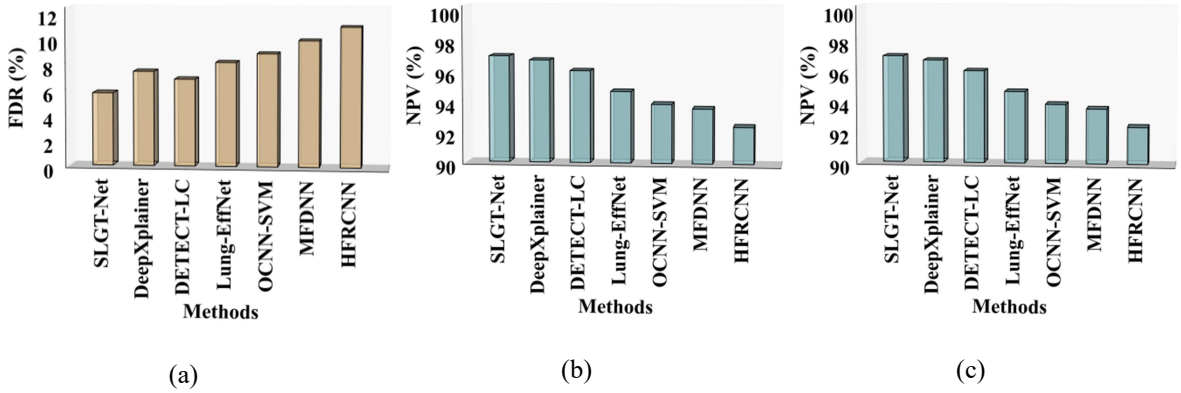

Figure 8: *Comparative analysis of (a) FNR (b) FDR (c) NPV*

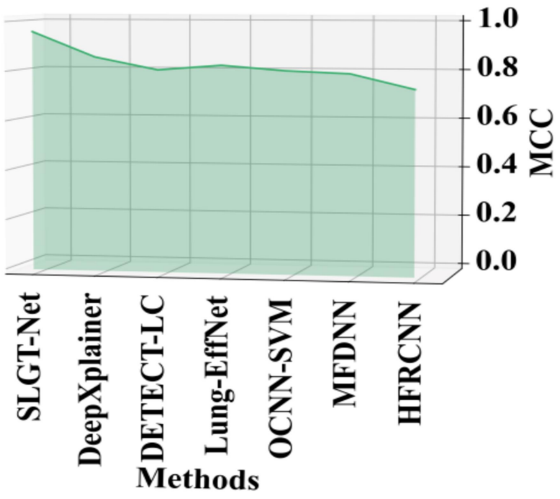

Figure 9: *Comparative analysis of MCC*

Table 6: *Ablation study of the components of SLGT-Net model*

Techniques	Evaluation measures									
	Accuracy (%)	**Precision (%)**	**Recall (%)**	**F1-score (%)**	**Specificity (%)**	**FPR (%)**	**FNR (%)**	**FDR (%)**	**NPV (%)**	**MCC**
Without preprocessing	90.36	91.32	91.56	91.43	89.12	10.88	8.44	6.11	92.31	0.75
Without data augmentation	89.32	86.33	89.25	87.76	83.26	16.74	10.75	12.56	85.23	0.68
Without feature extraction	74.63	73.47	76.25	74.83	69.25	30.75	23.75	14.56	75.23	0.56
Without TabNet	65.41	62.56	66.32	64.38	58.24	41.76	33.68	21.23	67.33	0.42
Without LightGBM	59.36	58.63	61.23	59.90	57.21	42.79	38.77	26.31	54.56	0.26
Overall efficiency	97.91	96.23	96.80	96.51	96.41	3.58	3.19	5.67	96.95	0.96

ISSN: 1992-8645 www.jatit.org E-ISSN: 1817-3195

Table 7: *McNamar's statistical test analysis*

Models	p-value
SLGT-Net	0.0147
DeepXplainer	0.0235
DETECT-LC	0.0362
Lung-EffNet	0.0388
OCNN-SVM	0.0421
MFDNN	0.0443
HFRCNN	0.0497